

pubs.acs.org/JACS Article

Understanding Ir(III) Photocatalyst Structure—Activity Relationships: A Highly Parallelized Study of Light-Driven Metal Reduction Processes

Stephen DiLuzio, Timothy U. Connell, Velabo Mdluli, Jakub F. Kowalewski, and Stefan Bernhard*



Cite This: J. Am. Chem. Soc. 2022, 144, 1431–1444



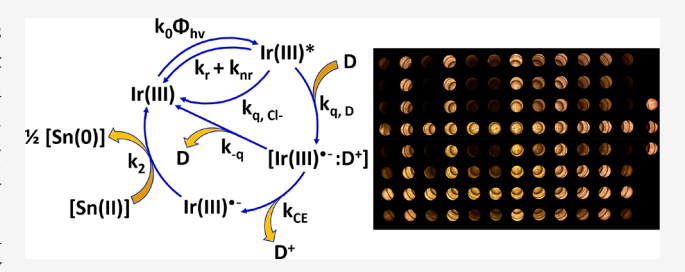
ACCESS I

Metrics & More

Article Recommendations

s Supporting Information

ABSTRACT: High-throughput synthesis and screening methods were used to measure the photochemical activity of 1440 distinct heteroleptic $[Ir(C^N)_2(N^N)]^+$ complexes for the photoreduction of Sn(II) and Zn(II) cations to their corresponding neutral metals. Kinetic data collection was carried out using home-built photoreactors and measured initial rates, obtained through an automated fitting algorithm, spanned between $0-120~\mu\text{M/s}$ for Sn(0) deposition and $0-90~\mu\text{M/s}$ for Zn(0) deposition. Photochemical reactivity was compared to photophysical properties previously



measured such as deaerated excited state lifetime and emission spectral data for these same complexes; however, no clear correlations among these features were observed. A formal photochemical rate law was then developed to help elucidate the observed reactivity. Initial rates were found to be directly correlated to the product of incident photon flux with three reaction elementary efficiencies: (1) the fraction of light absorbed by the photocatalyst, (2) the fraction of excited state species that are quenched by the electron donor, and (3) the cage escape efficiency. The most active catalysts exhibit high efficiencies for all three steps, and catalyst engineering requirements to maximize these elementary efficiencies were postulated. The kinetic treatment provided the mechanistic information needed to decipher the observed structure/function trends in the high-throughput work.

■ INTRODUCTION

Light absorption rapidly generates exceptionally reactive excited state species capable of converting photons into chemical energy for solar energy conversion, organic transformations, micropollutant degradation, CO2 reduction, and photodynamic therapy applications while circumventing the need for harsh reaction conditions or reagents. Following the example of nature, photochemical reactions can be initiated through absorption of visible light by a transition metal complex acting as a photocatalyst (PC). After Franck-Condon absorption upon illumination, internal conversion (IC) and, in some cases, intersystem crossing (ISC) results in the lowest energy excited state configuration (PC*). Deactivation of the PC* excited state can then occur via a reductive or oxidative electron transfer mechanism, offering the first step for transforming light into chemical energy. In a reductive quenching cycle, an electron donor (D) reduces the excited chromophore at rate k_q generating a highly reductive radical species PC -. A "dark' reaction subsequently takes place transferring that additional electron to an electron acceptor at a rate of k_2 , regenerating ground state PC and leaving behind an oxidized donor (D⁺) and reduced acceptor (A⁻) (Figure 1A).³⁶⁻³⁹ These sequential processes are the minimum required steps for photochemical energy storage; however, such diagrams are ambiguous in defining the rate limiting step for product turnover and mechanistic investigations in photocatalysis are largely underexplored and difficult to decipher. $^{40-44}$ More importantly, there is a growing body of evidence that the conventional three-step cycle is often a drastic oversimplification of real reaction mechanisms. $^{16,45-50}$

Suitable photosensitizers range from organic dyes to the historically used precious metal transition metal complexes containing Ru(II) and Ir(III) metal centers and, more recently, Earth abundant photocatalysts with Ni(II), Cu(I), Zr(IV), Fe(II), Mn(I), and W(VI) metal centers. $^{30,33,51-61}$ Heteroleptic d 6 [Ir(C^N) $_2$ (N^N)] $^+$ complexes (Figure 1B), where C^N is a cyclometalating ligand and N^N is an ancillary diimine ligand, regularly represent the gold standard in many applications due to (1) enhanced ligand field effects arising from the strong σ -donation of the cyclometalated carbanion, (2) the strong spin—orbit coupling of Ir allowing rapid population of long-lived triplet excited states, and (3) judicious tuning of frontier orbital energy levels through functional group modification on both C^N and N^N ligands.

Received: November 19, 2021 Published: January 13, 2022





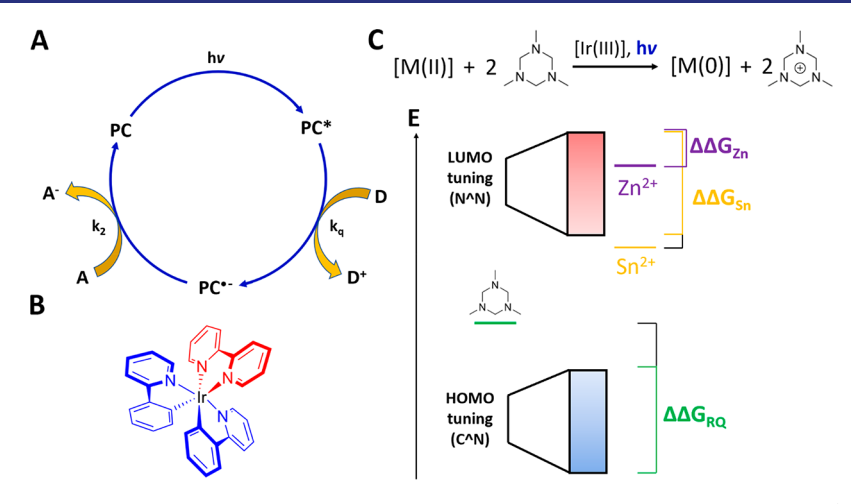


Figure 1. Conventional depiction of photocatalytic reaction cycles through a reductive quenching process (A). Archetypal heteroleptic $[Ir(C^N)_2(N^N)]^+$ complex with two cyclometalating ligands (blue) and one ancillary ligand (red) (B). The stoichiometric reaction mechanism studied in this work involves the photoreduction of metal salts (M = Sn, Zn) to neutral metals in the presence of 1,3,5-trimethylhexahydro-1,3,5-triazine as an electron donor and catalyzed by an Ir(III) photocatalyst and blue light (C). Depicted span of associated changes in the Gibbs free energy of reaction for the reductive quenching step ($\Delta\Delta G_{RQ}$, green) and electron transfers to Sn(II) and Zn(II) ($\Delta\Delta G_{Sn}$ (yellow), $\Delta\Delta G_{Zn}$ (purple)) achieved through frontier orbital energy level tuning (C). Black lines represent the minimal change in Gibbs free energy of these processes.

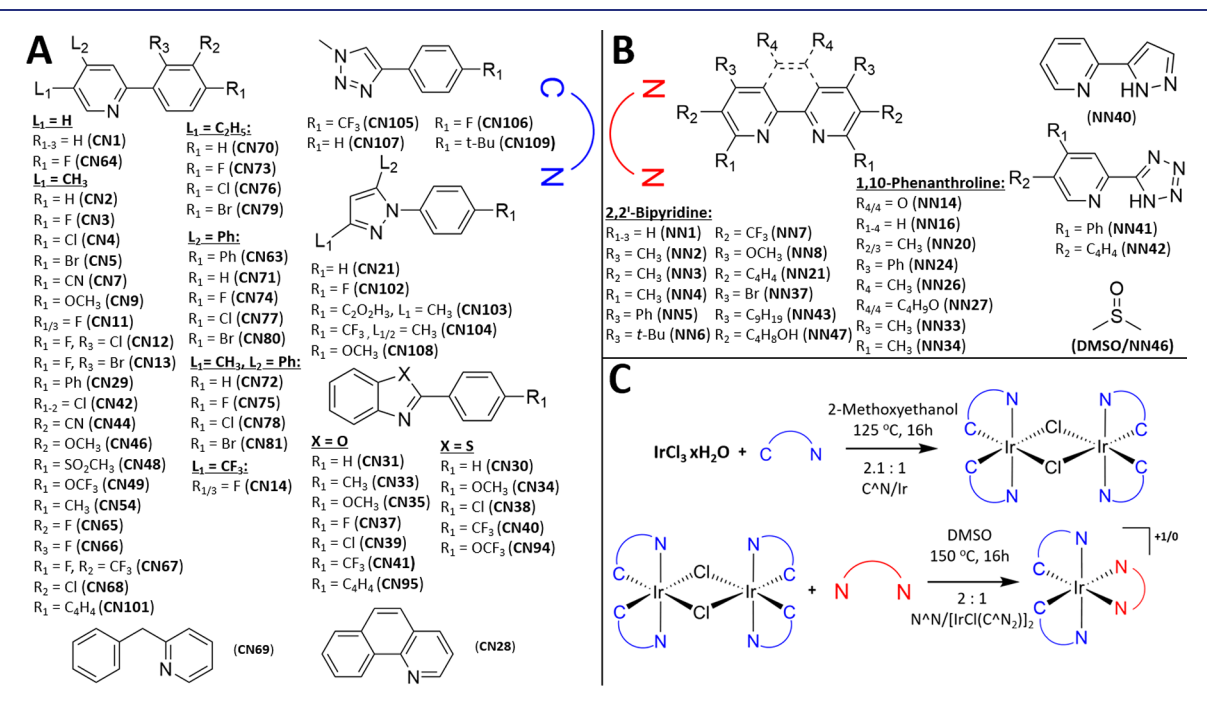


Figure 2. Scope of the combinatorial library. (A) Cyclometalating (C^N) and (B) ancillary (N^N) ligands used in library construction. Ligands are labeled using descriptors of a larger ligand library employed in our laboratory. Synthetic protocols for precursor $[Ir(Cl)(C^N)_2]_2$ dimers and high-throughput parallel synthesis of $[Ir(C^N)_2(N^N)]^+$ complexes (C). All ligand structures are shown in the Supporting Information (Tables S1 and S2).

Despite photochemistry's pervasiveness in the literature, correlating molecular structure/excited state configurations to photocatalyst activity is difficult to investigate and often explored only with a small selection of uniformly structured dyes. In order to understand wide-reaching structure—activity relationships, we use high-throughput synthesis and screening (HTSS) techniques to afford access to 1440 structurally diverse $[\text{Ir}(\text{C}^{\wedge}\text{N})_2(\text{N}^{\wedge}\text{N})]^+$ complexes. Our reaction of choice is the photoreduction of Sn(0) and Zn(0) from their corresponding Sn(II) and Zn(II) salts under uniform conditions using 1,3,5-trimethylhexahydro-1,3,5-triazine as an electron donor (D) (Figure 1C). Light-driven conversion of metal salts to their neutral metals represents an avenue for generating safe, energy

dense materials for solar energy conversion applications. ⁶⁹ Further, the modular synthesis of $[Ir(C^N)_2(N^N)]^+$ photocatalysts makes them a suitable model system to investigate structure—function relationships controlling photocatalytic activity as ligand modification changes both the excited state electronic structure and Gibbs free energy of each electron transfer event (Figure 1C, $\Delta\Delta G$). ^{70,71} This data set complements our previous work that characterized the photophysical properties (excited state lifetime, emission maximum, etc.) of these complexes to help elucidate how the electronic configuration of the excited state influences the measured photochemical activity. ⁷⁰ Combining these expansive data sets represents our efforts using high-throughput chemistry to

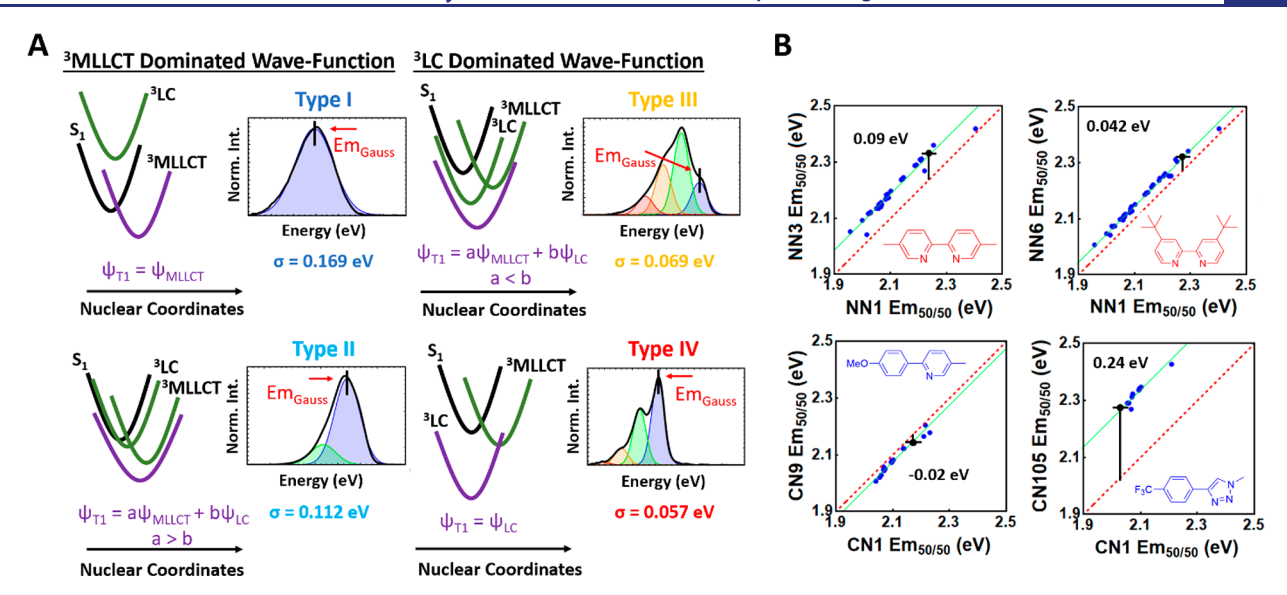


Figure 3. Depictions of four classes of excited state morphologies for heteroleptic $[Ir(C^N)_2(N^N)]^+$ complexes previously measured (A). The normalized emission spectra are fitted with Gaussian functions, where the highest energy peak from the Gaussian curves is called Em_{Gauss} (black, vertical line). The standard deviation (σ, eV) used to fit the data determines the excited state morphology and decreases from type I (3MLLCT) to type IV (3LC) spectral profiles. Representative plots used for determination of C^N 0 offset relative to CN1 and NN1 (B).

understand how molecular and electronic structure controls photocatalyst activity, working toward the development of wide reaching and data-driven correlations needed for creating robust chemical theory or machine learning models. ^{52,56,63,70–76} A kinetic equation for photoproduct formation was developed to help elucidate these sought after structure—activity relationships, providing the photocatalyst features needed to engineer the most active catalysts for creating novel solar energy conversion solutions.

■ INTRODUCTION TO [Ir(C^N)₂(N^N)]⁺ PHOTOPHYSICS

The frontier orbital structure in $[Ir(C^N)_2(N^N)]^+$ complexes constitutes a highest occupied molecular orbital (HOMO) localized on the Ir(III) d orbitals and the phenyl ring of the C^N ligand, while the lowest unoccupied molecular orbital (LUMO) is commonly centered on the ancillary ligand (Figure 1C). 65,660 Introducing electron withdrawing or rich ring systems either stabilizes or destabilizes the frontier orbitals, respectively. Given this spatial distribution, visible light transitions are found to be metal-ligand-to-ligand charge transfer (MLLCT, $d\pi_{C^{\Lambda}N} \rightarrow$ $\pi^*_{N^{\wedge}N}$). These transitions typically populate the ¹MLLCT state, where rapid rates of intersystem crossing and internal conversion subsequently yield the ³MLLCT state with high efficiencies. 65 If the π^* orbitals localized on the cyclometalating ligand are sufficiently stabilized, internal conversion from the ³MLLCT state to a ligand centered triplet state (³LC) will occur. 70 Prolonged excited state lifetimes are observed for 3LC states ($\geq 2 \mu s$), attributed to less metal character in the excited state, while ³MLLCT excited states are generally shorter lived. ³LC states are well characterized through emission spectral profiles depicting vibronic resolution, as $T_1 \rightarrow S_0$ is dominated by ${\pi^*}_{\mathsf{C}^\wedge\mathsf{N}} o \mathrm{d}\pi_{\mathsf{C}^\wedge\mathsf{N}}$ transitions, contrasting the structureless emission spectra of charge-separated ³MLLCT states. ⁷⁰ To investigate how ligand structure controls these photophysical properties, we developed an in situ synthetic protocol to afford 1440 structurally diverse $[Ir(C^N)_2(N^N)]^+$ complexes assembled from 60 cyclometalating ligands and 24 ancillary

ligands (the same ligands are used in this work). The ligand structures and synthetic protocols are depicted in Figure 2A/B and Figure 2C, respectively, while the reaction efficiency was previously discussed.⁷⁰

This previous work measured the deaerated excited state lifetime and emission spectra of all 1440 screened [Ir- $(C^{N})_{2}(N^{N})^{+}$ complexes, and we will quickly surmise the photophysical findings pertinent to the photochemical activity discussed here. First, four distinct excited state electron configurations were observed containing various degrees of mixing between the ³MLLCT and ³LC states (representative spectra are shown in Figure 3A) across the structurally diverse 60 C^N ligands and 24 N^N ligands tested (Figure 2A,B). Differentiation between these four types was determined by the fitting parameters of the spectral profile with Gaussian functions, primarily by the standard deviation (σ). We classified type I as pure ${}^{3}MLLCT$ ($\sigma = 0.169$ eV) and type IV as pure ${}^{3}LC$ ($\sigma =$ 0.057 eV), while types II and III are mixed electronic configurations where either ³MLLCT (type II) or ³LC (type III) dominates (Figure 3A). Vibronic substructure is clearly visible in both type III and type IV excited states, but the change in relative peak ratios between Em₀₋₀ and Em₀₋₁ indicates less nuclear reorganization in type IV following excitation. Second, the structural rigidity associated with 1,10-phenanthrolinebased compounds results in complexes with longer excited state lifetimes and higher energy emission attributed to a lack of torsional bond rotation between the pyridyl moieties in 2,2'bipyridine analogues occurring as a mode of internal conversion. Finally, a predictive model was built that measured the relative capacity to stabilize/destabilize the HOMO/LUMO energies of all ligands compared to parents 2-phenylpyridine (CN1) and 2,2'-bipyridine (NN1) (Figure 3B). For example, replacement of CN1 for the more electron deficient CN105 results in emission that was 0.24 eV higher in energy given the same N^N ligand (Figure 3B). In this previously published work, we labeled these offsets as C^N $_{\rm offset}$ and N^N $_{\rm offset}$. All C^N $_{\rm offset}$ and N^N $_{\rm offset}$ values are tabulated in the Supporting Information (Tables S3 and S4).

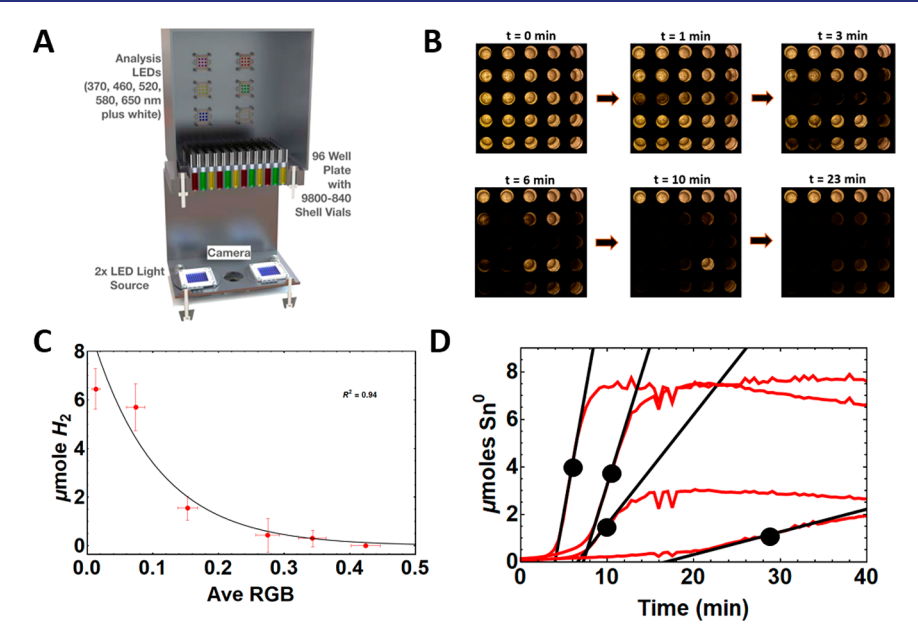


Figure 4. Diagram of the original photoreactor built to monitor 96 reactions under uniform conditions (A). Yellow analysis LEDs were most sensitive to metal precipitation and subsequently used. Example data collection traces of a 5 × 5 grid showing online monitoring of metal precipitation (B). Calibration curve used to transform raw RGB data to μ moles of neutral metal produced (C). The amount of H_2 produced was determined using GC following the reaction of conc. HCl with the photochemically reduced metal (see more in the Supporting Information) following the equation: $M^0 + 2H^+ \rightarrow H_2(g) + M^{2+}$, where M = Sn, Zn. Four sample traces for the photoreduction of Sn(0) (red) with automated initial rate fitting parameters (black), forming a linear fit at the onset of product formation (D). Traces represent four different Ir(III) photocatalysts.

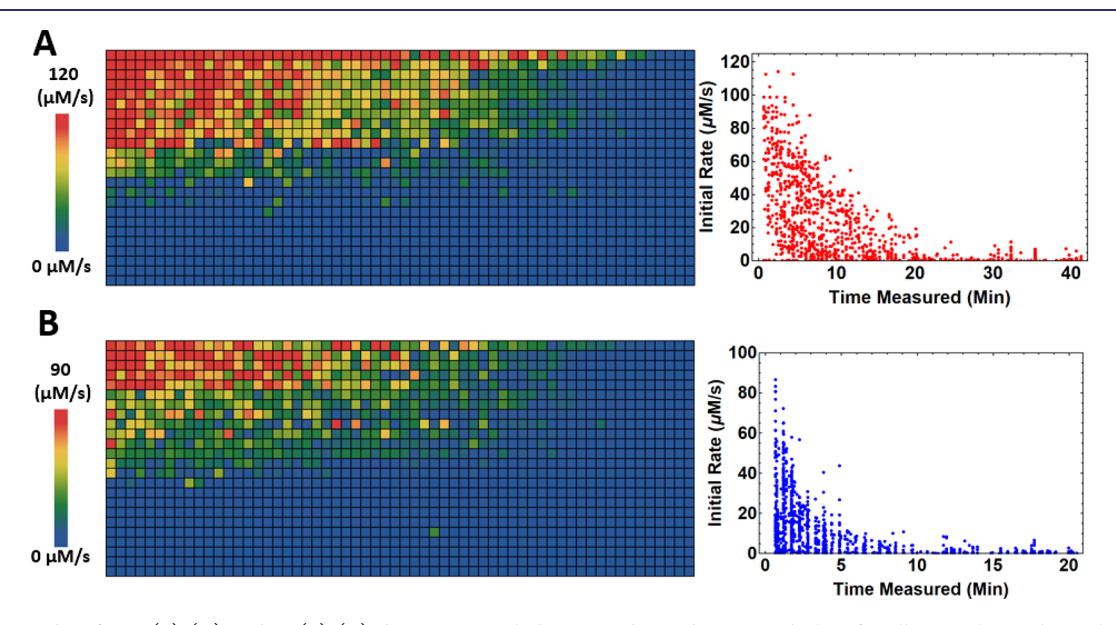


Figure 5. HTSS data for Sn(0) (A) and Zn(0) (B) deposition, including sorted two-dimensional plots for all 60 cyclometalating ligands and 24 ancillary ligands tested. Dependence of the initial rates of Sn(0) and Zn(0) deposition with the time in which the initial rate was measured (see black dots, Figure 4D, for four examples).

RESULTS AND DISCUSSION

Method of High-Throughput Photocatalytic Screening. The photoreduction of Sn(II) and Zn(II) to Sn(0) and Zn(0) was monitored through a previously described homebuilt photoreactor (Figure 4A), which allows online data collection during steady state illumination provided by two 100 W LEDs (440 nm) using a camera which photographs the 96 wells. The photoreactor is enclosed and the container is purged with an argon atmosphere for 2 h prior to illumination. Yellow LEDs above the reaction vials are turned on during data collection, while the strong blue illumination LEDs are switched

off to avoid saturating the camera (Figure 4B). As metal precipitates from the solution, the photographically measured RGB value per vial from the yellow light diminishes. RGB values were calibrated to moles of precipitated metal through GC quantification methods previously described (Figure 4C), and an exponential relationship was determined between the measured RGB value and the moles of metal produced. ⁶⁹ Initial rates were determined through fitting a linear equation at the onset of product formation (Figure 4D). A complete description of the calibration process, error analysis, and automated fitting can be found in the Supporting Information (pp S11–S17).

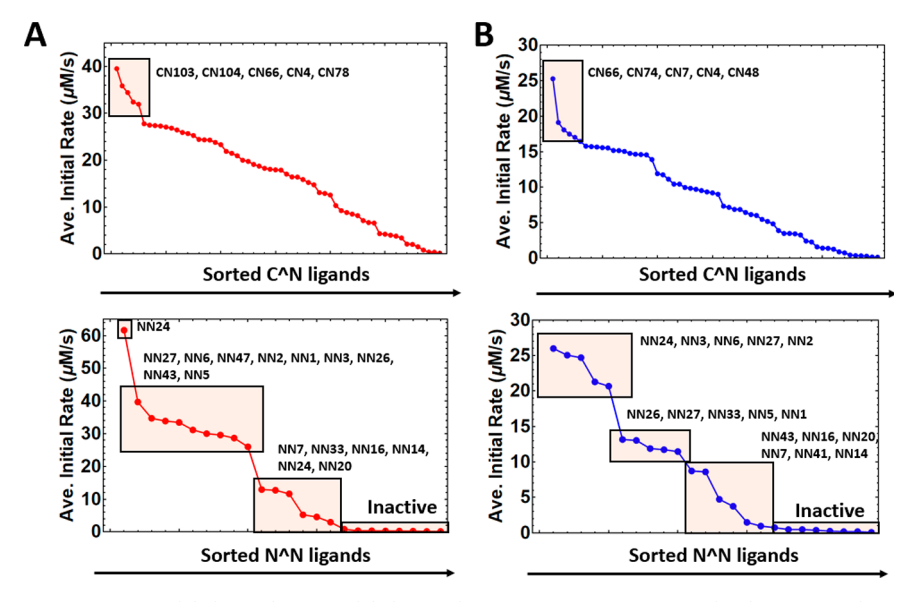


Figure 6. Sorted average initial rates for Sn(0) (A, red) and Zn(0) (B, blue) deposition based off C^N (top) and N^N (bottom) identity. Variation of C^N identity results in a near continuous change in the average most active to least active ligands, whereas variation of N^N identity yields abrupt discontinuities in reactivity when 1,10-phenathrolines are used compared to 2,2'-bipyridines. CN/NN labels next to each shaded region correspond to the ligands in that block.

Initial Rates of Sn(II) and Zn(II) Photoreduction. Initial rates for the photoreduction of Sn(II) and Zn(II) to their corresponding neutral metals ranged from 0–120 μ M/s for Sn(0) and 0–90 μ M/s for Zn(0) (Figure 5A,B). The magnitude of the initial rates and the time at which the initial rates were measured were strongly correlated (Figure 5A,B, right).

High-performing ligands were generally the same for both metals. For ancillary ligands, bathophenanthroline (NN24) showed the highest activity (Figure 6A,B) and many 2,2'bipyridine derivatives also performed well. A sharp decrease in initial rate occurred using rigid 1,10-phenanthroline derivatives (with the exception of NN24), while the negatively charged pyrazoles and tetrazoles were mostly inactive. Only electron rich 2,2'-bipyridine derivatives (NN2, NN3, NN6) remained highly active for Zn(0) formation. For cyclometalating ligands, slightly electron deficient 2-phenylpyridine and 1-phenylpyrazole derivatives were the best performers, whereas complexes containing 1-methyl-4-phenyl-1H-1,2,3-triazoles, 2-phenylbenzoxazoles, and 2-phenylbenzothiazoles showed moderate to low performance. Most electron rich cyclometalating ligands showed low performance regardless of ligand class. All average initial rates are included in the Supporting Information (Tables S5-S8).

As ligand properties clearly exhibit a strong influence on reactivity, we were interested in comparing the average initial rate of each ligand to its electronic effect on the frontier orbitals. Plots of C^N_{offset} vs the average initial rate for each C^N with all active N^N ligands are shown in Figure 7, where each plot point is color coded to represent the measured excited state electronic configuration (σ (eV), type I—type IV). For both Sn(0) and Zn(0) deposition, initial rates clearly increase as the excited state becomes a stronger photooxidant (increasing values of C^N_{offset}), attributed to a stronger quenching interaction between Ir(III)* and the amine donor (D). After reaching a HOMO stabilization of approximately 0.1 eV (relative to CN1), no increasing initial rates and clear correlation are observed. The peak observed at 0.1 eV coincides with a change in excited state morphology, where continued lowering of the HOMO energies

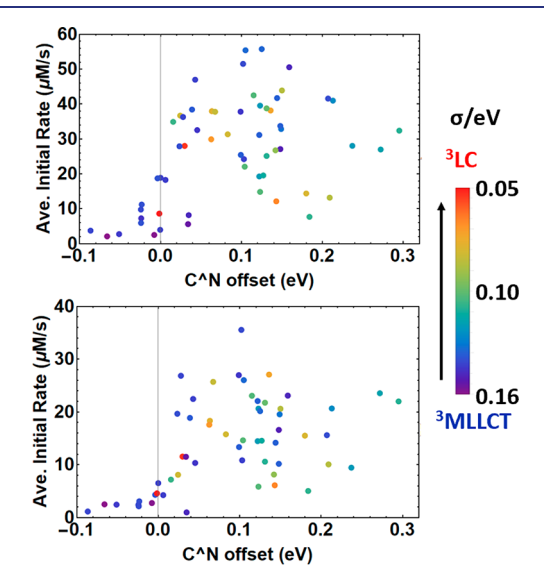


Figure 7. Plots of C^N_{offset} vs the average initial rate of product formation for Sn(0) (top) and Zn(0) (bottom). Plots are color coded based on the average sigma (eV) value for each C^N ligand used for fitting the emission spectra.

yields excited states with increased ³LC character (types II–IV). It therefore appears that excited state mixing, which reduces the charge transfer nature of the excited state, negatively impacts initial rates, although there are still type I ³MLLCT (blue dots) excited states that also exhibit low reactivity. The same general trend is observed for Zn(0) deposition (Figure 7, bottom). Conversely, although Figure 6 shows clear differences in reactivity dependent on N^N ligand identity, no clear correlations between N^Noffset and the average N^N-based rate can be determined (Figure S6). The lack of correlations based off N^Noffset is counterintuitive, as the promoted electron on these Ir(III) chromophores is predominantly located on this ligand, and this finding suggests that the reduction potential of

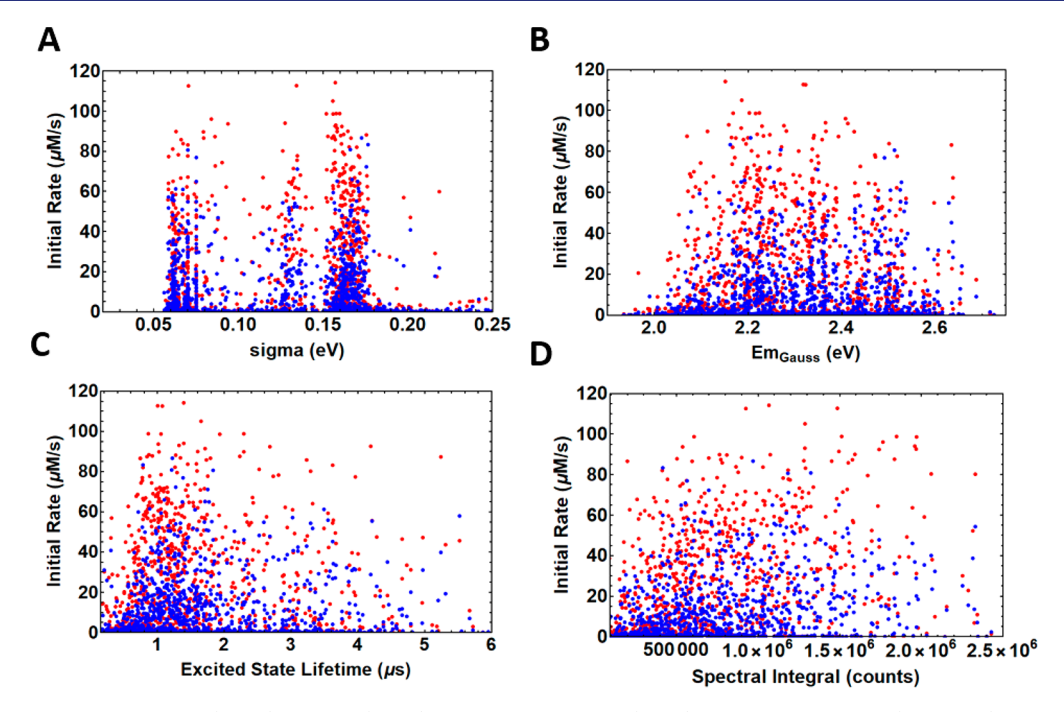


Figure 8. Correlations between sigma (eV, A), Em_{Gauss} (eV, B), excited state lifetime (μ s, C), and spectral integral (counts, D) to initial rates of M(0) deposition. (M = Sn (red), Zn (blue)) measured using the HTSS protocol.

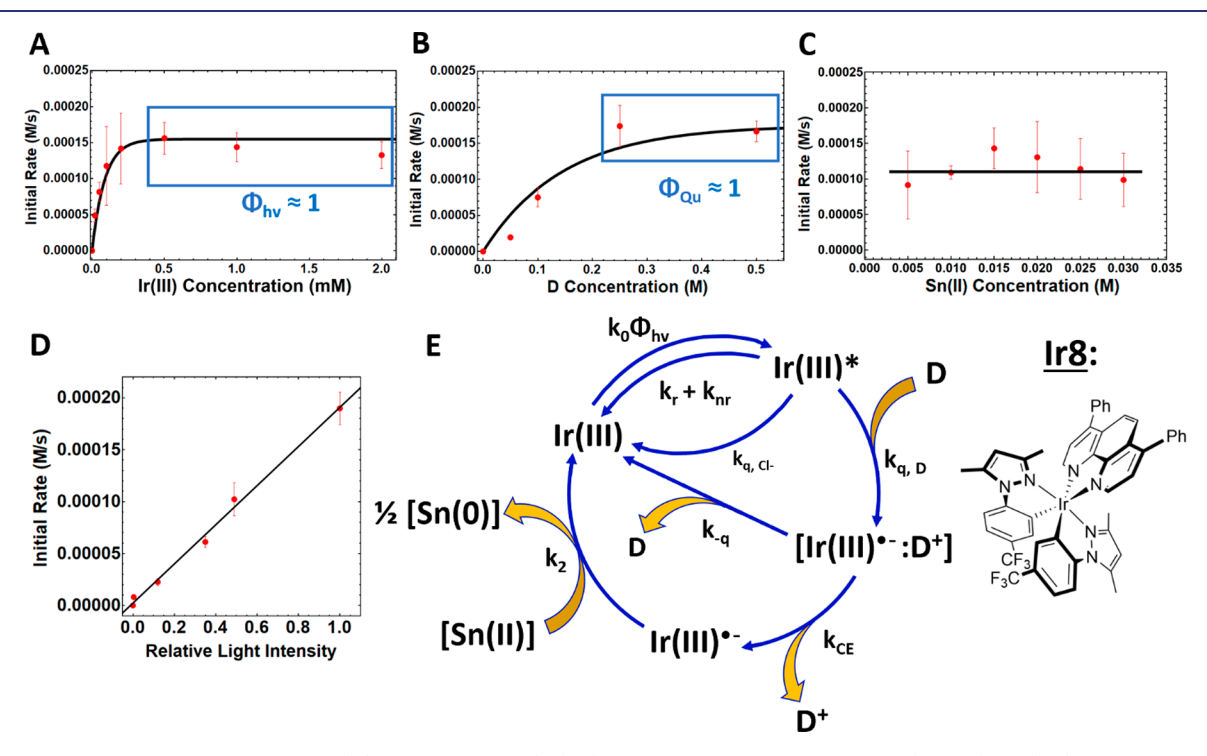


Figure 9. Dependence of the initial rate of Sn(0) formation on [Ir(III)] (A, [D] = 0.5 M, [SnCl₂] = 0.025 M), [D] (B, [Ir(III)] = 0.2 mM, [SnCl₂] = 0.025 M), [Sn(II)] (C, [Ir(III)] = 0.2 mM, [D] = 0.25 M), and relative light intensity (D). These data are consistent with the depicted scheme in part E using **Ir8** as the photocatalyst (structure shown). The data in parts A and B are fitted to the equation: Initial Rate = m(1-10^{-α[M]}), where *m* is the initial rate observed when Φ_{hv} and Φ_{Qu} = 1 (blue squares), [M] is the concentration of either [Ir(III)] (A) or [D] (B), and α is the parameter that controls the [Ir(III)] or [D] in which Φ_{hv} and Φ_{Qu} = 1. Larger values of α result in the plateaus in A and B observed at lower Ir(III) and D concentrations.

the complex is less impactful on the metal deposition initial rates than expected.

To aid in explaining these observed trends, we compared the metal reduction data to the photophysical property database generated in our previous work. ⁷⁰ Surprisingly, the variance in the measured initial rates for Sn(0) and Zn(0) deposition

spanned the variance in the measured photophysical properties (Sigma (eV), $\rm Em_{Gauss}$, (eV, Figure 3A), excited state lifetime (μs), and spectral integral (counts)), implying no direct correlations between any measured photophysical property and chemical reactivity (Figure 8). While it does appear that complexes with low emission energy (~ 2.0 eV), short lifetime

(<0.5 μ s), and weak emission integral (<150,000 counts) are substantially disadvantaged, chemical reactivity is largely uncorrelated once this lower photophysical property threshold is met. Apparently the relationship between excited state electronic configuration and reactivity (Figure 8A) is not straightforward.

The lack of apparent trends between the measured photophysical properties and ligand-based reactivity suggests a more complicated reaction mechanism than absorption and subsequent electron-transfer-based exergonicity of the reductive quenching and "dark" electron transfer steps. Moreover, none of the above data explains why initial rates of metal deposition decrease with Ir(III) photocatalysts containing the structurally rigid 1,10-phenanthroline ligands relative to 2,2'-bipyridine analogues. We therefore decided to develop a system of kinetic equations consistent with experimental observation that may elucidate the reaction mechanism and reveal why rigidity and excited state mixing diminishes reactivity.

Photochemical Kinetics. For this purpose, a much more detailed kinetic analysis was performed on 22 traditionally synthesized and isolated $[Ir(C^N)_2(N^N)]^+$ complexes (labeled Ir1-Ir22, their structures are shown in the Supporting Information, Table S9), spanning the range of photophysical and photochemical space. Our high-throughput photoreactor enabled us to generate unprecedented amounts of raw kinetic data measuring initial rates as a function of reagent and photocatalyst concentration as well as light intensity. Figure 9 summarizes the general observed behavior across the entire 22complex data set (data points represent the average initial rate over three experiments, with error bars equivalent to the standard deviation). While the initial rate revealed a hyperbolic dependence with varying [Ir(III)] and [D] (Figure 9A,B), a zeroth order dependence on [Sn(II)] was observed (Figure 9C). A linear relationship with respect to light intensity (Figure 9D) indicated a single-photon process across the measured light intensities.⁴¹ A coordination equilibrium between D and the Zn(II) ions was discovered (Supporting Information, pp S53 and S54); therefore, Sn(0) data is presented for simplicity, although both reactions follow the same trends. Complete data sets for Sn(0) and Zn(0) deposition utilizing Ir1-Ir22 are presented in the Supporting Information (Figures S7–S12). Control experiments confirmed that all components (light, Ir(III), D, and Sn(II)/Zn(II) are required for Sn(0) or Zn(0)precipitation.

The data presented in Figure 9A–D for Ir8 coincides with the scheme in Figure 9E. The presented pathways are consistent with a rate law expression for the formation of Sn(0) that follows eq 1

$$\frac{\mathrm{d}[\mathrm{Sn}(0)]}{\mathrm{d}t} = k_{\mathrm{o}} \Phi_{h\nu} \Phi_{\mathrm{Qu}} \Phi_{\mathrm{CE}} \tag{1}$$

where k_0 is the incident irradiation intensity with units Einsteins/s (1 mol of photons = 1 Einstein). The photocatalyst transforms moles of photons into moles of product, allowing the unit conversion to M/s for initial rates. $\Phi_{h\nu}$ represents the fraction of light absorbed by the photocatalyst and is related to the transmission of the solution: $\Phi_{h\nu}$ approaches 1 as transmission approaches zero, representing the [Ir(III)] where all incident light is absorbed (Figure 9A). The rate of excitation can be described as the product $k_0 \cdot \Phi_{h\nu}$ (Figure 9E). $\Phi_{Q\mu}$ is the fraction of Ir(III)* quenched by D and approaches 1 when all excited species are quenched at rate k_q (Figure 9B). Φ_{CE} is the cage escape efficiency and represents the efficiency of

forming Ir(III) • after each quenching event. The formation of Ir(III) - is not equivalent to excited state quenching, as unproductive back-electron transfer reforms the ground state complex at rate k_{-q} (thermally converting the absorbed photon energy (Figure 9E)). Generating $Ir(III)^{\bullet-}$ occurs at rate k_{CE} from a charge-separated encounter complex, [Ir(III) •-: D+], formed following the reductive quenching of Ir(III)* by D but before Ir(III) - and D+ diffuse away from each other. Interestingly, the actual process of transforming the metal ion to metallic solid is not reflected in eq 1, which is a consequence of the zeroth order dependence on the initial rate of [Sn(II)] (Figure 9C). Kinetically, these three efficiencies can be accessed by a steady state approximation with respect to the intermediates shown in Figure 9E (Ir(III)*, [Ir(III)*-:D+], Ir(III) - and light; a full description of the kinetic model is provided in the Supporting Information (pp S48-S52).

According to eq 1, the rate of product (Sn(0)) formation is directly proportional to the rate of photon absorption $(k_0 \cdot \Phi_{hv})$ multiplied by the fraction of each intermediate that productively continues along the photochemical cycle in Figure 9E. The rate of a photochemical reaction with external quantum efficiency equal to 1 (where all incident photons generate the photoproduct, i.e., $\Phi_{h\nu} = \Phi_{Qu} = \Phi_{CE} = 1$) necessarily equals the rate of photon flux. Any deviation between the measured reaction rate and k_0 arises from photons that do not generate $Ir(III)^{\bullet - .77}$ For an absorbed photon to yield the photoproduct, Ir(III)* must be quenched and then form Ir(III) -; however, both of these critical intermediates can unproductively decay back to ground state Ir(III) at rates $k_r + k_{nr}$ or k_{-q} , respectively. The zeroth order dependence of the initial rate of Sn(0) formation on [Sn(II)]suggests that, once Ir(III) • is formed, it quantitatively transfers an electron to Sn(II) (Supporting Information, pp S48-S52). Consequently, the product of these three elementary efficiencies represents the external quantum efficiency and highly active photocatalysts exhibit the largest numerical value for this product.

The importance of $\Phi_{ ext{CE}}$ is apparent when comparing the initial rate of Sn(0) formation for different photocatalysts. If the rate of excited state quenching matched the rate of Ir(III) • formation, there would be no difference in initial rates between different photocatalysts when $\Phi_{hv} = \Phi_{Ou} = 1$ (plateaus in the blue boxes of Figure 9A,B) given quantitative electron transfer from Ir(III) •to the metal ion (as confirmed by zeroth order dependence on [Sn(II)]). This saturated region is observed across all photocatalysts (Figure 10 and Figures S7, S8, S10, and S11 in the Supporting Information), and it is apparent that differences in observed initial rates still persist at [Ir(III)] and [D], where $\Phi_{h\nu}$ = Φ_{Ou} = 1. The discrepancy observed must arise due to differences in the rate of generation of Ir(III). as all Ir photocatalysts tested exhibit a zeroth order dependence of the initial rate of Sn(0) formation on [Sn(II)], suggesting that the elementary step lowering initial rates occurs after excited state quenching but before Ir(III) - formation and that Ir(III) - is not degrading over the time scales in which initial rates were measured (Supporting Information, pp S48-S52). 78,79 A notable complex is Ir22, which exhibits minimal catalytic activity across all concentration ranges tested, despite strong absorption at the irradiation wavelength and a quenching interaction with D (Figure S13, Table 1).

The Absorption Elementary Efficiency, Φ_{hv} . Starting with excitation, Φ_{hv} is determined with the equation used to fit the data $(1-10^{-\alpha[Ir(III)]})$ in Figures 9A/10A. This elementary efficiency is a function of [Ir(III)] and approaches 1 as [Ir(III)]

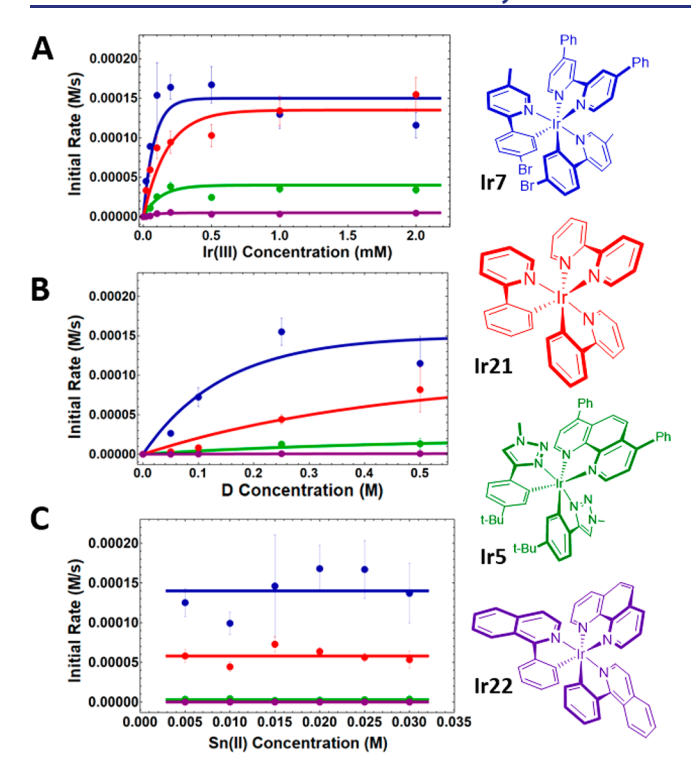


Figure 10. Dependence of the initial rate of Sn(0) formation on [Ir(III)] (A), [D] (B), and [Sn(II)] (C) with Ir5, Ir7, Ir21, and Ir22. The reaction conditions were the same as those in Figure 9.

is increased, in accordance with Beer's law. Tabulated values of $\Phi_{h\nu}$ are included in Table 1 at [Ir(III)] = 0.2 mM. The fitting parameter, α , describes how the initial rate of Sn(0) deposition

depends on [Ir(III)]. Increasingly larger values of α (units [M]⁻¹) indicate a stronger capability of a photocatalyst to absorb the incident irradiation, and correspondingly, enhancing the molar absorptivity of the photocatalysts for the irradiation wavelength strongly controls the [Ir(III)] at which $\Phi_{h\nu}$ approaches 1. This is experimentally observed, as complexes with larger molar absorptivities (ε_0) approach an independence of the initial rate of Sn(0) deposition on [Ir(III)] at lower concentrations of photocatalyst, exemplified by a plot of α against ε_0 of all 22 Ir(III) photocatalysts (Figure 11A). Increasing absorptivity can be achieved by either lowering the HOMO-LUMO gap through synthetic tuning or using highly conjugated C^N or N^N ligands. 80,81 For example, despite the opposite electronics of the C^N ligand of Ir5 (electron rich, with a tert-butyl substituted phenyl ring, Figure 10) and Ir8 (electron poor, with a -CF₃ substituted phenyl ring, Figure 9), their respective molar absorptivities at 440 nm are very similar (Table 1), attributed to the highly conjugated bathophenanthroline ancillary ligand. This is a particularly useful characteristic, as it allows photocatalysts to possess both potent excited state reduction potentials and large molar absorptivity in the visible region.

The Excited State Quenching Elementary Efficiency, Φ_{Qu} . To investigate the effect of Φ_{Qu} , we measured the excited state lifetime of each photocatalyst and the Stern–Volmer quenching rate constants for all species initially present in solution (D, SnCl₂). Φ_{Qu} is formally calculated using eq 2 (Supporting Information, pp S48–S52)

$$\Phi_{Qu} = \frac{k_{q,D}[D]}{k_r + k_{nr} + k_{q,D}[D] + k_{q,Cl}[Cl]}$$
(2)

Table 1. Tabulated Values for $k_r + k_{nr}$ (Equal to the Decay of the Excited State), $k_{q,D}$, $k_{q,Cl-}$, $\Phi_{h\nu}$, Φ_{Qu} , and Φ_{CE} for All 22 $[Ir(C^N)_2(N^N)]^+$ Complexes^a

	$\varepsilon_{\rm o}$ @ 440 nm (M $^{-1}$ cm $^{-1}$)	$k_{\rm r} + k_{\rm nr} \times 10^6 \; ({\rm s}^{-1})$	$k_{\rm (q,D)} \times 10^6 \; ({ m M}^{-1} \; { m s}^{-1})$	$k_{\rm (q,Cl-)} \times 10^6 ({\rm M}^{-1} {\rm s}^{-1})$	$\Phi(hv)^b$	$\Phi(Qu)^c$	norm. $\Phi(CE)_{Rel}^{d}$
Ir1	1880	1.32	0.91	3.29	0.75	0.24	0.22
Ir2	1320	0.51	180.96	158.19	0.37	0.95	0.21
Ir3	750	3.16	5.68	53.77	0.21	0.39	0.21
Ir4	2740	1.75	5.62	23.30	0.80	0.55	0.28
Ir5	1610	1.33	0.25	3.01	0.80	0.08	0.02
Ir6	1030	3.67	1.10	2.34	0.21	0.13	0.02
Ir7	2080	1.37	45.60	43.25	0.92	0.90	0.98
Ir8	2260	0.58	51.44	102.51	0.90	0.89	1.00
Ir9	600	1.09	22.70	36.47	0.87	0.85	0.43
Ir10	1570	0.30	20.61	113.84	0.60	0.77	0.78
Ir11	1930	0.97	36.49	44.62	0.92	0.90	0.81
Ir12	40	0.08	0.03	1.14	0.0	0.13	0.00
Ir13	1360	3.84	194.66	48.82	0.37	0.95	0.00
Ir14	200	0.77	66.23	100.52	0.75	0.91	0.26
Ir15	880	0.67	188.82	192.04	0.75	0.95	0.85
Ir16	530	0.40	4.46	195.52	0.37	0.30	0.02
Ir17	890	0.68	84.97	105.72	0.87	0.93	0.67
Ir18	270	0.36	100.32	188.73	0.68	0.91	0.79
Ir19	5840	0.36	2.29	5.28	0.97	0.70	0.46
Ir20	4260	0.06	0.02	0.55	0.60	0.13	0.01
Ir21	1730	2.82	3.31	6.33	0.68	0.36	0.35
Ir22	7750	0.28	1.74	0.04	0.90	0.76	0.03

 $^{^{}a}k_{\text{q,D}}$ and $k_{\text{q,Cl}}$ are the measured Stern–Volmer quenching rate constants. Φ_{hv} is calculated from the experimental fits to the data in Figure 9A (1– $10^{-a[\text{Ir}(III)]}$), and Φ_{Qu} is calculated using eq 2. $^{b}\Phi_{hv}$ is calculated for all photocatalysts at 0.2 mM concentrations. $^{c}\Phi_{\text{Qu}}$ is calculated at [D] = 0.5 M and SnCl₂ = 0.025 M. $^{d}\Phi_{\text{CE}}(\text{Rel})$ was determined using Ir22 as the reference and normalized to Ir8.

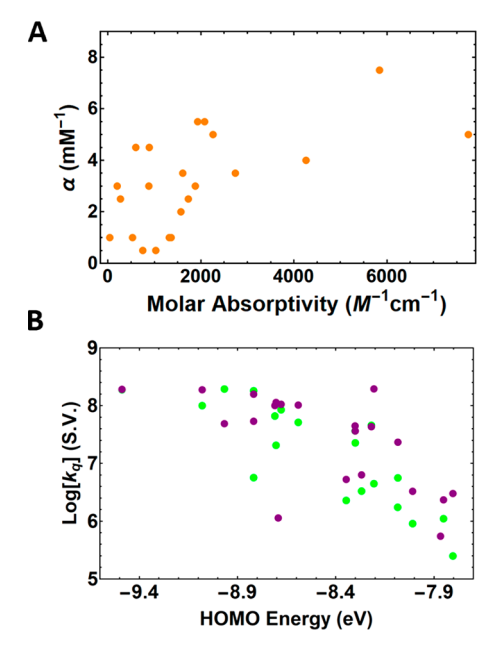


Figure 11. Relationship between the fits obtained (α, mM^{-1}) in Figure 9A/10A and Figure S7 to the molar absorptivity (ε_0) (Table 1) of the Ir(III) photocatalysts tested in this work (A). Complexes with a higher probability of incident irradiation absorption achieved an independence of the initial rate of Sn(0) formation on [Ir(III)] at lower concentrations of photocatalyst (with larger values of α). Logarithmic dependence on the Stern-Volmer quenching rate constants for 1,3,5trimethylhexahydro-1,3,5-triazine (green) and SnCl₂ (purple) in DMSO on the DFT calculated HOMO energy levels at the PW6B85D3 level of theory using the LANL2DZ basis set (B).

where $k_{\rm r}$ and $k_{\rm nr}$ are the associated radiative and non-radiative rate constants controlling excited state deactivation and $k_{q,D}$ and $k_{q,Cl}$ are the measured Stern-Volmer quenching rate constants for D and Cl-, respectively. All rate constants are tabulated in Table 1. When $\Phi_{Qu} = 1$, all generated $Ir(III)^*$ is quenched by D. This occurs when $k_{q,D}[D] \gg k_r + k_{nr} + k_{q,Cl}[Cl^-]$, showing a dependence of Φ_{Qu} on [D] (consistent with the observed hyperbolic behavior in Figure 9B). The values of the quenching rate constants span 4 orders of magnitude and strongly correlate with the calculated DFT HOMO orbital energy levels (Figure 11B, green). Φ_{Qu} can therefore approach 1 by stabilizing HOMO orbital energy levels to increase $k_{q,D}$, affording photocatalysts with more positive excited state reduction potentials, or enhancing the excited state lifetime (which lowers $k_{\rm r}$ and $k_{\rm nr}$). The phosphorescence of the Ir photocatalysts was also quenched in the presence of SnCl₂, exhibiting the same dependence on the magnitude of the quenching rate constants when compared to HOMO orbital energy levels (Figure 11B, purple). We attribute this to a reductive quenching cycle occurring from chloride in solution, as no quenching is observed when the chloride is replaced with the trifluoromethanesulfonate anion, indicating the quenching is not originating from the Sn(II) cation (Figure S14). It is important to note that this excited state quenching process does not produce Ir(III) - in solution, and consequently only results in reformation of ground state Ir(III) (Figure 9E, Supporting Information, pp S48–S52), as control experiments indicated no Sn(0) formation without the presence of D.

The Cage Escape Elementary Efficiency, Φ_{CE} . Φ_{CE} quantifies the efficiency of Ir(III) - generation after the generation of a charge-separated encounter complex, [Ir(III) •-: D⁺], which can be formed at a rate quantified by the Stern-Volmer quenching study. 82 The electronic configuration of the involved species is depicted in Figure 12. [Ir(III)•-:D+]

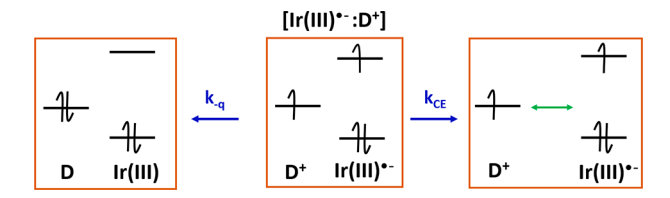


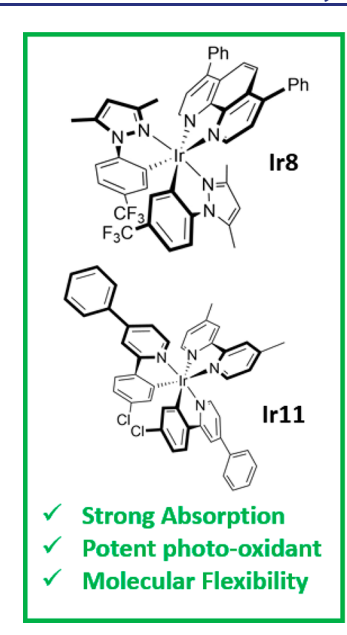
Figure 12. Proposed electronic structure of the charge-separated encounter complex ([Ir(III)*-:D+]) with associated back-electron transfer (k_{-a}) reforming ground state electronic configurations. The green arrow represents the diffusion of D⁺ and Ir(III) • away from each other, escaping the solvent cage.

productively decays at rate $k_{\rm CE}$ to release free ${\rm Ir}({\rm III})^{ullet-}$ in solution. Φ_{CE} is calculated using eq 3:

$$\Phi_{\rm CE} = \frac{k_{\rm CE}}{k_{\rm CE} + k_{\rm -q}} \tag{3}$$

If $k_{\rm CE} \gg k_{\rm -q}$, then $\Phi_{\rm CE}$ approaches 1 and the rate of formation of $Ir(III)^{\bullet-}$ equals the rate of excited state quenching (k_a) ; however, back-electron transfer, alternatively called charge recombination, is often competitive and reduces Φ_{CE} . Although these processes are not diffusion limited, the associated back-electron transfer can be a spin-forbidden process given the electronic configuration depicted in Figure 12. In this case, a spin change would be required to reform Ir(III) and D, given the triplet dominated wave function of $Ir(III)^*.^{70,84}$ While understanding the factors affecting Φ_{CE} are difficult, approaches to influence spin—orbit coupling have been shown to change k_{-q} . So Further, Coulombic attraction between donor-acceptor species also alters cage escape efficiencies, but this attraction is absent with these 1,3,5-trimethylhexahydro-1,3,5-triazine/ $[Ir(C^N)_2(N^N)]^+$ couples, as no ion pairing is expected. 87 Although Φ_{CE} cannot be measured explicitly without knowledge of the photon flux (k_0) , the relative Φ_{CE} can be determined with respect to a single photocatalyst when $\Phi_{h\nu}$ and Φ_{Qu} are calculated (Table 1). We used Ir22 as our reference catalyst and normalized $\Phi_{\text{CE}}(\text{Rel})$ across the 22complex set to Ir8.

Our high-throughput data suggests an alternative approach to control k_{-a} : As D and Ir(III)* approach each other, D is in a relaxed, uncharged geometry and Ir(III)* is in the relaxed T₁ geometry after thermal relaxation through internal conversion and intersystem crossing. ^{64,65,68} At a particular distance, an electronic transfer occurs from D to Ir(III)*, forming the chargeseparated encounter complex [Ir(III) • -: D+]. This forward electron transfer appears to lie within the Marcus normal region, as their rates increase with increasing exothermicity of the electron transfer event (Figure 11B). The associated, undesired back-electron transfer reduces D+, which regenerates ground state D and should not have a significant kinetic barrier assuming that back-electron transfer happens faster than degradation pathways commonly observed for oxidized tertiary amines.⁹⁸ This step has been shown to exist within the Marcus inverted region.⁹⁵ Different photocatalysts appear to have different reorganization energies controlling the activation energy of this electron transfer, where a decreased Marcus reorganization energy would be expected if similarities in equilibrium geometries exist between Ir(III) - and Ir(III).



- ✓ Weak Absorption
 ✓ Potent photo-oxidant
 ✓ Molecular Flexibility
 ✓ Moderate Absorption
 ✓ Weak photo-oxidant
- ✓ Weak Absorption
 ✓ Weak photo-oxidant
 ✓ Molecular Rigidity
 ✓ Strong Absorption
 ✓ Weak photo-oxidant
 ✓ Molecular Rigidity

Figure 13. Example Ir photocatalysts that are highly active (green, Ir8, Ir11), moderately active (yellow, Ir14, Ir21), and minimally reactive (red, Ir16, Ir22).

Molecular Flexibility

Our previous work describing how C^N and N^N ligands control nuclear reorganization may help elucidate a photocatalyst's capacity to reorganize while cycling through the different intermediates of a photochemical cycle. The rigidity of 1,10-phenanthroline N^N derivatives (Figure 2B) affords complexes with stronger emission intensity, longer excited state lifetimes, and higher energy emission maximums. While these rigid ligands offer advantageous photophysical properties, they also hinder photocatalytic activity; minimal reorganization energy likely promotes back-electron transfer in the encounter complex, resulting in relatively low Φ_{CE} efficiencies for Ir2, Ir4, Ir14, Ir16, Ir20, and Ir22 (Table 1) and consequently minimal photocatalyst activity. The emission spectral profile reveals that Ir2, Ir20, and Ir22 are all type IV excited states (3LC with dominant Em₀₋₀ emission band, Figure 3A), indicating similar equilibrium geometries of T₁ and S₀ (Figure S13).⁷⁰ This hindered nuclear reorganization ability likely persists with Ir(III) --, thereby reducing the Marcus reorganization energy and facilitating larger back-electron transfer rate constants for the [Ir(III) • -: D+] encounter complex. Finally, complexes with large relative Φ_{CE} efficiencies all have flexible molecular structures (Ir7, Ir8, Ir9, Ir11, Ir15, and Ir18). The phenyl rings on the ancillary ligands of Ir7 and Ir8 (Figures 9 and 10) can act as a mode of nuclear reorganization that results in different equilibrium geometries of the Ir(III) and Ir(III) •species. Further, the phenyl ring bound to the pyridyl moiety on the C^N ligand of Ir11 likely also results in geometrical changes after excitation. Ir18 exhibits a type III spectral profile, indicating large geometric differences between T₁ and S₀ (Figure S13). The greater Φ_{CE} efficiencies of Ir9 and Ir15 can be rationalized through the lack of rigidity associated with the 2,2'-bipyridine N^N ancillary ligand, where torsional bond rotation occurring as a mode of internal conversion (IC) changes the T₁ and S₀ equilibrium geometries.⁷⁰ The trends observed among this diverse set of catalysts suggest that rapid charge recombination, which depends on nuclear reorganization of the Ir(III) photocatalyst, strongly influences cage escape efficiency.

Overall Observed Photocatalyst Activity. Equation 1 shows that highly active photocatalysts possess ligand features maximizing the product of the three associated elementary efficiencies ($\Phi_{h\nu}$, Φ_{Qu} , and Φ_{CE}). Examples of highly active Ir photocatalysts are shown in Figure 13 (green box), where the extended π systems of the C^N/N^N ligands, halogenated C^N ligands, and pendant phenyl rings afford the necessary enhanced absorption, excited state reduction potential, and cage escape efficiency. Moderately active photocatalysts (Figure 13, yellow box) often possess the structural features advantageous for one or two of these elementary efficiencies, but not all of them. Finally, poor photocatalysts almost exclusively exhibit disadvantageous features for at least two elementary efficiencies (weak absorption, less positive excited state reduction potentials, or ligands with rigid molecular structure) (Figure 13, red box).

Revisiting the HTSS Data. Equation 1 can be used to qualitatively understand the observed metal deposition rates across the HTSS. The observed increasing initial rates of Sn(0)and Zn(0) deposition with larger C^Noffset likely arise through increasing the Φ_{Ou} elementary efficiency. The maximum activity was observed for ligands with $C^N_{offset} \approx 0.1$ eV, offsets greater than this typically produced decreased rates (Figure 7). This decrease could be attributed to lowering $\Phi_{h\nu}$ —stabilizing the HOMO hypsochromically shifts the absorption spectra—or less charge separation in mixed excited states, therefore facilitating back-electron transfer in the encounter complex. As the excited state becomes ³LC dominated (transiting from type II to type IV), the HSOMO and LSOMO are spatially localized exclusively on the C^N ligand. As the oxidation of the amine (D) is more likely to occur as it approaches this ligand, the spatial proximity between the HSOMO and D⁺ formed after quenching could result in more electronic orbital overlap, resulting in higher rates of k_{-q} . The decreased initial rates for complexes containing 1,10-phenanthroline analogues likely suffer from low Φ_{CE} as the structural rigidity of these N^N ligands also ensures similar geometries between Ir(III) and $Ir(III)^{\bullet -}$, facilitating k_{-q} independent of excited state morphology. We rationalize the high efficiencies of NN5 and NN24 to

phenyl ring rotation which ensures significantly different geometries between T1 and S0. Further, the extended conjugation of NN24 affords stronger absorption in the visible region, likely facilitating larger values for Φ_{hv} . Phenyl ring rotation also rationalizes why CN70-CN81 (Figure 2A) are active C^N ligands: the phenyl ring on the pyridyl moiety of the C^N ligand does not strongly impact the frontier orbital energies and the thermodynamics of the electron transfer, but the added molecular flexibility aids the necessary change in geometry required for high Φ_{CE} . Further, the general observation that the same ligands are active for both Sn(0) and Zn(0) deposition suggests the observed initial rates are strongly correlated to these structural considerations, and not to the reactivity of Ir(III) • and the cations. The fact that the actual metal cation reduction dark reaction does not impact the overall rate of this process is surprising. Although the kinetics indicate that Ir(III) - transfers an electron to the cationic species, the mechanism of metal precipitation could proceed through a dimeric species or a disproportionation reaction.⁶⁹ Notably, the kinetic formulation supports that any of these mechanisms are fast and do not influence the measured catalyst activity.

CONCLUSIONS

A high-throughput synthesis and screening protocol was developed to measure the initial rate of Sn(II) and Zn(II) photoreduction to their neutral metals for 1440 heteroleptic $[Ir(C^N)_2(N^N)]^+$ photocatalysts. Catalyst activity was compared to previously measured photophysical properties, but no clear correlation could be determined. A kinetic equation was formulated to understand the reaction mechanism, where the initial rate is directly proportional to the rate of photon flux multiplied by three elementary efficiencies: (1) incident light absorption (Φ_{hv}) , (2) quenching the photocatalyst excited state (Φ_{Qu}) , and (3) the cage escape efficiency (Φ_{CE}) . These elementary efficiencies present a picture of photochemical reaction progress (Figure 9E) much more complicated than the typical standard three-step cycle depicted in Figure 1A and are crucial toward understanding photocatalyst activity. Ligand structural rigidity is correlated to cage escape efficiency and suppression of back-electron transfer/charge recombination, where differences in equilibrium nuclear positioning between Ir(III)*/Ir(III)*- and Ir(III) modulate the Marcus reorganization energy controlling the kinetic barrier for back-electron transfer. Notably, these elementary efficiencies controlling photocatalyst activity are seemingly uncorrelated to conventional photophysical features presented in Figure 8. These findings allow feature selection for highly active photocatalysts capable of maximizing the conversion of light in solar fuels or for pinpointing efficient photoredox catalysis.

EXPERIMENTAL SECTION

High-Throughput Synthetic Protocol. Synthesis and characterization of all cyclometalating ligands and their chloro-bridged dimers is described elsewhere. ⁷⁰ To a solution of 100 μ L of 0.5 mM iridium dimer in DMSO was added 100 μ L of 1.0 mM N^N ancillary ligand in DMSO. Reactions were performed on a 96-well synthesis plate, described previously. ^{70,71} The reaction vessel was heated to 150 °C for 16 h.

Sn Deposition Procedure. After cooling the 96-well synthesis plate, to each glass vial containing 200 μ L of a 0.5 mM unique heteroleptic [Ir(C^N)₂(N^N)]⁺ complex was added 300 μ L of a 40 mL DMSO stock solution containing 1.2 mL of hexahydro-1,3,5-trimethyl-1,3,5-triazine (D) and 316.0 mg of anhydrous SnCl₂, yielding final solution compositions of 128.0 mM hexahydro-1,3,5-trimethyl-1,3,5-

triazine, 25.0 mM $SnCl_2$, and 0.2 mM $[Ir(C^N)_2(N^N)]^+$ complex. After addition, the vials were sealed and mixed in the absence of light.

Zn Deposition Procedure. After cooling the 96-well synthesis plate, to each glass vial containing 200 μ L of a 0.2 mM unique heteroleptic [Ir(C^N)₂(N^N)]⁺ complex, 300 μ L of a 40 mL DMSO stock solution containing 1.2 mL of hexahydro-1,3,5-triazine and 3.002 g of anhydrous ZnBr₂ was added. This yields a final solution compositions of 128.0 mM hexahydro-1,3,5-triazine, 0.2 M ZnBr₂, and 0.2 mM [Ir(C^N)₂(N^N)]⁺ complex. After addition, the vials were sealed and mixed in the absence of light.

Photophysical Measurements. The traditionally prepared iridium(III) complexes were irradiated as a 0.2 mM solution in DMSO with a pulsed 365 nm LED, powered by a 40 ns square pulse from a Siglent SDG1052 function generator. Emission was detected with a Hamamatsu H7732-11 photomultiplier tube connected to a Tektronix TDS3032B digital oscilloscope interfaced to a Raspberry Pi 3 Model B+ computer. Scattered light from the excitation source was removed from acquired spectra using a plexiglass filter (365 nm long pass). Emission spectra were measured concurrently using a StellarNet BLACK-Comet concave grating spectrometer and collected with spectral correction of spectrometer sensitivity.

Computational Modeling. Electronic structure was modeled with singlet density functional theory (DFT) through geometry optimization at the PW6B85D3 level of theory using the LANL2DZ basis set on Gaussian 16

Absorption Spectra. UV—vis absorption spectra were collected with a Shimadzu UV-1800 spectrophotometer in $0.1~\mathrm{mM}$ aerated DMSO solutions.

Illumination Intensity Reactions. Ir8 was employed as the photocatalyst for intensity dependent reactions due to its exceptional reactivity. Four different neutral density filters were placed over the 100 W blue illumination LEDs, and reaction progress for the photodeposition of Sn metal was monitored with a solution composition of 25.0 mM SnCl₂, 213.4 mM hexahydro-1,3,5-trimethyl-1,3,5-triazine, and 0.2 mM Ir8 in DMSO. Relative filtering capacity was determined by monitored changes in spectral integral when the filter was placed between an illumination LED and a StellarNet BLACK-Comet concave grating spectrometer and collected without spectral correction of spectrometer sensitivity.

Stern–Volmer Analysis. Time-resolved and steady state Stern–Volmer analysis was performed using 0.2 mM solutions **Ir1–Ir21** with hexahydro-1,3,5-trimethyl-1,3,5-triazine (0, 0.025, 0.05, 0.125, 0.25, and 0.5 M) in deaerated DMSO and fit to the following equations

$$\tau_{\rm o}/\tau = 1 + K_{\rm sv}[{\rm D}]$$
 and $I_{\rm o}/I = 1 + K_{\rm sv}[{\rm D}]$

where τ represents the time-resolved lifetime in the presence (τ) and absence (τ_0) of quencher and I represents the integrated emission spectra in the presence (I) and absence (I_0) of quencher.

ASSOCIATED CONTENT

Supporting Information

The Supporting Information is available free of charge at https://pubs.acs.org/doi/10.1021/jacs.1c12059.

All supporting figures and tables (PDF)

Extracted features from Gaussian fitting (XLSX)

AUTHOR INFORMATION

Corresponding Author

Stefan Bernhard — Department of Chemistry, Carnegie Mellon University, Pittsburgh, Pennsylvania 15213, United States; orcid.org/0000-0002-8033-1453; Email: bern@cmu.edu

Authors

Stephen DiLuzio — Department of Chemistry, Carnegie Mellon University, Pittsburgh, Pennsylvania 15213, United States

- Timothy U. Connell Department of Chemistry, Carnegie Mellon University, Pittsburgh, Pennsylvania 15213, United States; orcid.org/0000-0002-6142-3854
- **Velabo Mdluli** Department of Chemistry, Carnegie Mellon University, Pittsburgh, Pennsylvania 15213, United States
- Jakub F. Kowalewski Department of Chemistry, Carnegie Mellon University, Pittsburgh, Pennsylvania 15213, United States

Complete contact information is available at: https://pubs.acs.org/10.1021/jacs.1c12059

Notes

The authors declare no competing financial interest.

ACKNOWLEDGMENTS

We are grateful for the financial support of the US NSF (CHE-2102460). NMR instrumentation at Carnegie Mellon University was partially supported by the NSF (CHE-1039870 and CHE-1726525).

REFERENCES

- (1) Wang, Y.; Zheng, C.; Liu, M.; Wei, W.; Gao, J.; Zhang, Y.; Deng, P. Anchoring Ir(III) complex on macroscopic polymer substrate as highly durable photosensitizer for photocatalytic hydrogen evolution. *ChemComm.* **2021**, *57* (32), 3857–3860.
- (2) Huang, J.; Sun, J.; Wu, Y.; Turro, C. Dirhodium(II,II)/NiO Photocathode for Photoelectrocatalytic Hydrogen Evolution with Red Light. *J. Am. Chem. Soc.* **2021**, *143* (3), 1610–1617.
- (3) Zhou, Y.; He, P.; Mo, X. F.; Liu, C.; Gan, Z. L.; Tong, H. X.; Yi, X. Y. Neutral CyclometalatedIr(III) Complexes with Pyridylpyrrole Ligand for Photocatalytic Hydrogen Generation from Water. *Inorg. Chem.* **2021**, *60* (9), *6266*–*6275*.
- (4) Whittemore, T. J.; Xue, C.; Huang, J.; Gallucci, J. C.; Turro, C. Single-chromophore single-molecule photocatalyst for the production of dihydrogen using low-energy light. *Nat. Chem.* **2020**, *12* (2), 180–185.
- (5) Call, A.; Franco, F.; Kandoth, N.; Fernandez, S.; Gonzalez-Bejar, M.; Perez-Prieto, J.; Luis, J. M.; Lloret-Fillol, J. Understanding light-driven H₂ evolution through the electronic tuning of aminopyridine cobalt complexes. *Chem. Sci.* **2018**, *9* (9), 2609–2619.
- (6) Khnayzer, R. S.; Thoi, V. S.; Nippe, M.; King, A. E.; Jurss, J. W.; El Roz, K. A.; Long, J. R.; Chang, C. J.; Castellano, F. N. Towards a comprehensive understanding of visible-light photogeneration of hydrogen from water using cobalt(II) polypyridyl catalysts. *Energy Environ. Sci.* **2014**, *7* (4), 1477–1488.
- (7) Giannoudis, E.; Benazzi, E.; Karlsson, J.; Copley, G.; Panagiotakis, S.; Landrou, G.; Angaridis, P.; Nikolaou, V.; Matthaiaki, C.; Charalambidis, G.; Gibson, E. A.; Coutsolelos, A. G. Photosensitizers for H₂ Based on Charged or Neutral Zn and Sn Porphyrins. *Inorg. Chem.* **2020**, *59* (3), 1611–1621.
- (8) Mills, I. N.; Porras, J. A.; Bernhard, S. Judicious Design of Cationic, Cyclometalated Ir(III) Complexes for Photochemical Energy Conversion and Optoelectronics. *Acc. Chem. Res.* **2018**, *51* (2), 352–364.
- (9) Ackerman, L. K. G.; Martinez Alvarado, J. I.; Doyle, A. G. Direct C-C Bond Formation from Alkanes Using Ni-Photoredox Catalysis. *J. Am. Chem. Soc.* **2018**, *140* (43), 14059–14063.
- (10) De Abreu, M.; Belmont, P.; Brachet, E. Light-Enabled Radical 1,4-Aryl Migration Via a Phospho-Smiles Rearrangement. *J. Org. Chem.* **2021**, *86* (*5*), 3758–3767.
- (11) Rupp, M. T.; Auvray, T.; Shevchenko, N.; Swoboda, L.; Hanan, G. S.; Kurth, D. G. Substituted 2,4-Di(pyridin-2-yl)pyrimidine-Based Ruthenium Photosensitizers for Hydrogen Photoevolution under Red Light. *Inorg. Chem.* **2021**, *60* (1), 292–302.
- (12) Qin, J.; Zhu, S.; Chu, L. Dual Photoredox-/Palladium-Catalyzed Cross-Electrophile Couplings of Polyfluoroarenes with Aryl Halides and Triflates. *Organometallics.* **2021**, 40 (14), 2246–2252.

- (13) Zhang, Y.; Petersen, J. L.; Milsmann, C. A Luminescent Zirconium(IV) Complex as a Molecular Photosensitizer for Visible Light Photoredox Catalysis. *J. Am. Chem. Soc.* **2016**, *138* (40), 13115–13118.
- (14) Zhang, Z.; Ngo, D. T.; Nagib, D. A. Regioselective Radical Amino-Functionalizations of Allyl Alcohols via Dual Catalytic Cross-Coupling. ACS Catal. 2021, 11 (6), 3473–3477.
- (15) Jiang, H.; Yu, X.; Daniliuc, C. G.; Studer, A. Three-Component Aminoarylation of Electron-Rich Alkenes by Merging Photoredox with Nickel Catalysis. *Angew. Chem., Int. Ed.* **2021**, *60* (26), 14399–14404.
- (16) Qin, Y.; Sun, R.; Gianoulis, N. P.; Nocera, D. G. Photoredox Nickel-Catalyzed C-S Cross-Coupling: Mechanism, Kinetics, and Generalization. *J. Am. Chem. Soc.* **2021**, *143* (4), 2005–2015.
- (17) Xu, J.; Yang, Y.; Zhao, X.; Liu, C.; Zhang, D. DFT Mechanistic Study of Ir(III)/Ni(II)-Metallaphotoredox-Catalyzed Difluoromethylation of Aryl Bromides. *Inorg. Chem.* **2021**, *60* (12), 8682–8691.
- (18) Prier, C. K.; Rankic, D. A.; MacMillan, D. W. Visible light photoredox catalysis with transition metal complexes: applications in organic synthesis. *Chem. Rev.* **2013**, *113* (7), 5322–5363.
- (19) Griffin, J. D.; Zeller, M. A.; Nicewicz, D. A. Hydrodecarboxylation of Carboxylic and Malonic Acid Derivatives via Organic Photoredox Catalysis: Substrate Scope and Mechanistic Insight. *J. Am. Chem. Soc.* **2015**, *137* (35), 11340–11348.
- (20) Pistritto, V.; Schutzbach-Horton, M.; Nicewicz, D. Nucleophilic Aromatic Substitution of UnactivatedFluoroarenes Enabled by Photoredox Catalysis. *J. Am. Chem. Soc.* **2020**, *142* (40), 17187–17194.
- (21) Devery III, J. J.; Douglas, J. J.; Nguyen, J. D.; Cole, K. P.; Flowers II, R. A.; Stephenson, C. R. J. Ligand functionalization as a deactivation pathway in a *fac*-Ir(ppy)₃-mediated radical addition. *Chem. Sci.* **2015**, *6* (1), 537–541.
- (22) Nagib, D. A.; MacMillan, D. W. Trifluoromethylation of arenes and heteroarenes by means of photoredox catalysis. *Nature.* **2011**, *480*, 224–228.
- (23) Zheng, S.; Zhang, S.-Q.; Saeednia, B.; Zhou, J.; Anna, J. M.; Hong, X.; Molander, G. A. Diastereoselective olefin amidoacylation via photoredox PCET/nickel-dual catalysis: reaction scope and mechanistic insights. *Chem. Sci.* **2020**, *11* (16), 4131–4137.
- (24) Porras, J. A.; Mills, I. N.; Transue, W. J.; Bernhard, S. Highly Fluorinated Ir(III)-2,2':6',2''-Terpyridine-Phenylpyridine-X Complexes via Selective C-F Activation: Robust Photocatalysts for Solar Fuel Generation and Photoredox Catalysis. *J. Am. Chem. Soc.* **2016**, *138* (30), 9460–9472.
- (25) Shon, J. H.; Kim, D.; Rathnayake, M. D.; Sittel, S.; Weaver, J.; Teets, T. S. Photoredox catalysis on unactivated substrates with strongly reducing iridium photosensitizers. *Chem. Sci.* **2021**, *12* (11), 4069–4078
- (26) Giedyk, M.; Narobe, R.; Weiß, S.; Touraud, D.; Kunz, W.; König, B. Photocatalytic activation of alkyl chlorides by assembly-promoted single electron transfer in microheterogeneous solutions. *Nat. Catal.* **2020**, 3 (1), 40–47.
- (27) Tian, L.; Till, N. A.; Kudisch, B.; MacMillan, D. W. C.; Scholes, G. D. Transient Absorption Spectroscopy Offers Mechanistic Insights for an Iridium/Nickel-Catalyzed C-O Coupling. *J. Am. Chem. Soc.* **2020**, *142* (10), 4555–4559.
- (28) Pfund, B.; Steffen, D. M.; Schreier, M. R.; Bertrams, M. S.; Ye, C.; Borjesson, K.; Wenger, O. S.; Kerzig, C. UV Light Generation and Challenging Photoreactions Enabled by Upconversion in Water. *J. Am. Chem. Soc.* **2020**, *142* (23), 10468–10476.
- (29) Kerzig, C.; Guo, X.; Wenger, O. S. Unexpected Hydrated Electron Source for Preparative Visible-Light Driven Photoredox Catalysis. J. Am. Chem. Soc. 2019, 141 (5), 2122–2127.
- (30) Zhang, X.; Cibian, M.; Call, A.; Yamauchi, K.; Sakai, K. Photochemical CO₂ Reduction Driven by Water-Soluble Copper(I) Photosensitizer with the Catalysis Accelerated by Multi-Electron Chargeable Cobalt Porphyrin. *ACS Catal.* **2019**, *9* (12), 11263–11273. (31) Cheong, H. Y.; Kim, S. Y.; Cho, Y. J.; Cho, D. W.; Kim, C. H.;
- Son, H. J.; Pac, C.; Kang, S. O. Photosensitization Behavior of Ir(III) Complexes in Selective Reduction of CO_2 by Re(I)-Complex-

- Anchored TiO₂ Hybrid Catalyst. *Inorg. Chem.* **2017**, 56 (19), 12042–12053.
- (32) Genoni, A.; Chirdon, D. N.; Boniolo, M.; Sartorel, A.; Bernhard, S.; Bonchio, M. Tuning Iridium Photocatalysts and Light Irradiation for Enhanced CO₂ Reduction. *ACS Catal.* **2017**, *7* (1), 154–160.
- (33) Cheung, P. L.; Kapper, S. C.; Zeng, T.; Thompson, M. E.; Kubiak, C. P. Improving Photocatalysis for the Reduction of CO_2 through Non-covalent Supramolecular Assembly. *J. Am. Chem. Soc.* **2019**, *141*, 14961–14965.
- (34) Huang, H.; Banerjee, S.; Sadler, P. J. Recent Advances in the Design of Targeted Iridium(III) Photosensitizers for Photodynamic Therapy. *Chembiochem.* **2018**, *19* (15), 1574–1589.
- (35) Karges, J.; Heinemann, F.; Jakubaszek, M.; Maschietto, F.; Subecz, C.; Dotou, M.; Vinck, R.; Blacque, O.; Tharaud, M.; Goud, B.; VinuelasZahi Nos, E.; Spingler, B.; Ciofini, I.; Gasser, G. Rationally Designed Long-Wavelength Absorbing Ru(II) Polypyridyl Complexes as Photosensitizers for Photodynamic Therapy. *J. Am. Chem. Soc.* **2020**, 142 (14), 6578–6587.
- (36) Capaldo, L.; Ravelli, D. The Dark Side of Photocatalysis: One Thousand Ways to Close the Cycle. *Eur. J. Org. Chem.* **2020**, 2020 (19), 2783–2806.
- (37) Bevernaegie, R.; Wehlin, S. A. M.; Elias, B.; Troian-Gautier, L. A Roadmap Towards Visible Light Mediated Electron Transfer Chemistry with Iridium(III) Complexes. *ChemPhotoChem* **2021**, *5* (3), 217–234.
- (38) Tucker, J. W.; Stephenson, C. R. Shining light on photoredox catalysis: theory and synthetic applications. *J. Org. Chem.* **2012**, *77* (4), 1617–1622.
- (39) Buzzetti, L.; Crisenza, G. E. M.; Melchiorre, P. Mechanistic Studies in Photocatalysis. *Angew. Chem., Int. Ed.* **2019**, 58 (12), 3730–3747.
- (40) Targos, K.; Williams, O. P.; Wickens, Z. K. Unveiling Potent Photooxidation Behavior of Catalytic Photoreductants. *J. Am. Chem. Soc.* **2021**, *143* (11), 4125–4132.
- (41) Xu, J.; Cao, J.; Wu, X.; Wang, H.; Yang, X.; Tang, X.; Toh, R. W.; Zhou, R.; Yeow, E. K. L.; Wu, J. Unveiling Extreme Photoreduction Potentials of Donor-Acceptor Cyanoarenes to Access Aryl Radicals from Aryl Chlorides. *J. Am. Chem. Soc.* **2021**, *143* (33), 13266–13273.
- (42) Marchini, M.; Bergamini, G.; Cozzi, P. G.; Ceroni, P.; Balzani, V. Photoredox Catalysis: The Need to Elucidate the Photochemical Mechanism. *Angew. Chem., Int. Ed.* **2017**, *56* (42), 12820–12821.
- (43) Ghosh, I.; Shaikh, R. S.; Konig, B. Sensitization-Initiated Electron Transfer for Photoredox Catalysis. *Angew. Chem., Int. Ed.* **2017**, *56* (29), 8544–8549.
- (44) Ghosh, I.; Bardagi, J. I.; Konig, B. Reply to "Photoredox Catalysis: The Need to Elucidate the Photochemical Mechanism. *Angew. Chem., Int. Ed.* **2017**, *56* (42), 12822–12824.
- (45) Connell, T. U.; Fraser, C. L.; Czyz, M. L.; Smith, Z. M.; Hayne, D. J.; Doeven, E. H.; Agugiaro, J.; Wilson, D. J. D.; Adcock, J. L.; Scully, A. D.; Gomez, D. E.; Barnett, N. W.; Polyzos, A.; Francis, P. S. The Tandem Photoredox Catalysis Mechanism of [Ir(ppy)₂(dtb-bpy)]⁺ Enabling Access to Energy Demanding Organic Substrates. *J. Am. Chem. Soc.* **2019**, *141* (44), 17646–17658.
- (46) Czyz, M. L.; Taylor, M. S.; Horngren, T. H.; Polyzos, A. Reductive Activation and Hydrofunctionalization of Olefins by Multiphoton Tandem Photoredox Catalysis. *ACS Catal.* **2021**, *11* (9), 5472–5480.
- (47) Forni, J. A.; Micic, N.; Connell, T. U.; Weragoda, G.; Polyzos, A. Tandem Photoredox Catalysis: Enabling Carbonylative Amidation of Aryl and Alkylhalides. *Angew. Chem., Int. Ed.* **2020**, 59 (42), 18646—18654.
- (48) Nicholls, T. P.; Robertson, J. C.; Gardiner, M. G.; Bissember, A. C. Identifying the potential of pulsed LED irradiation in synthesis: copper-photocatalysed C-F functionalisation. *ChemComm.* **2018**, *54* (36), 4589–4592.
- (49) Kudisch, M.; Lim, C. H.; Thordarson, P.; Miyake, G. M. Energy Transfer to Ni-Amine Complexes in Dual Catalytic, Light-Driven C-N Cross-Coupling Reactions. J. Am. Chem. Soc. 2019, 141 (49), 19479—19486.

- (50) Stevenson, B. G.; Spielvogel, E. H.; Loiaconi, E. A.; Wambua, V. M.; Nakhamiyayev, R. V.; Swierk, J. R. Mechanistic Investigations of an alpha-AminoarylationPhotoredox Reaction. *J. Am. Chem. Soc.* **2021**, 143 (23), 8878–8885.
- (51) Yeung, K.; To, W.; Sun, C.; Cheng, G.; Ma, C.; Tong, G.; Tang, C.; Che, C. Luminescent Tungsten(VI) Complexes: Photophysics and Applicability to Organic Light-Emitting Diodes and Photocatalysis. *Angew. Chem. Int.* **2017**, *56*, 133–137.
- (\$2) Motz, R. N.; Lopato, E. M.; Connell, T. U.; Bernhard, S. High-Throughput Screening of Earth-Abundant Water Reduction Catalysts toward Photocatalytic Hydrogen Evolution. *Inorg. Chem.* **2021**, *60* (2), 774–781.
- (53) Woodhouse, M. D.; McCusker, J. K. Mechanistic Origin of Photoredox Catalysis Involving Iron(II) Polypyridyl Chromophores. *J. Am. Chem. Soc.* **2020**, *142* (38), 16229–16233.
- (54) Rosemann, N. W.; Chabera, P.; Prakash, O.; Kaufhold, S.; Warnmark, K.; Yartsev, A.; Persson, P. Tracing the Full Bimolecular Photocycle of Iron(III)-Carbene Light Harvesters in Electron-Donating Solvents. *J. Am. Chem. Soc.* **2020**, *142* (19), 8565–8569.
- (55) Zhang, Y.; Petersen, J. L.; Milsmann, C. A Luminescent Zirconium(IV) Complex as a Molecular Photosensitizer for Visible Light Photoredox Catalysis. *J. Am. Chem. Soc.* **2016**, *138* (40), 13115—13118.
- (56) Goldsmith, J. I.; Hudson, W. R.; Lowry, M. S.; Anderson, T. H.; Bernhard, S. Discovery and High-Throughput Screening of Heteroleptic Iridium Complexes for Photoinduced Hydrogen Production. *J. Am. Chem. Soc.* **2005**, 127 (20), 7502–7510.
- (57) Zhang, Y.; Lee, T. S.; Favale, J. M.; Leary, D. C.; Petersen, J. L.; Scholes, G. D.; Castellano, F. N.; Milsmann, C. Delayed fluorescence from a zirconium(IV) photosensitizer with ligand-to-metal charge-transfer excited states. *Nat. Chem.* **2020**, *12* (4), 345–352.
- (58) Shields, B. J.; Kudisch, B.; Scholes, G. D.; Doyle, A. G. Long-Lived Charge-Transfer States of Nickel(II) Aryl Halide Complexes Facilitate Bimolecular Photoinduced Electron Transfer. *J. Am. Chem. Soc.* **2018**, *140* (8), 3035–3039.
- (59) Ting, S. I.; Garakyaraghi, S.; Taliaferro, C. M.; Shields, B. J.; Scholes, G. D.; Castellano, F. N.; Doyle, A. G. ³d-d Excited States of Ni(II) Complexes Relevant to Photoredox Catalysis: Spectroscopic Identification and Mechanistic Implications. *J. Am. Chem. Soc.* **2020**, 142 (12), 5800–5810.
- (60) Minozzi, C.; Caron, A.; Grenier-Petel, J. C.; Santandrea, J.; Collins, S. K. Heteroleptic Copper(I)-Based Complexes for Photocatalysis: Combinatorial Assembly, Discovery, and Optimization. *Angew. Chem., Int. Ed.* **2018**, *57* (19), 5477–5481.
- (61) Herr, P.; Kerzig, C.; Larsen, C. B.; Häussinger, D.; Wenger, O. S. Manganese(I) complexes with metal-to-ligand charge transfer luminescence and photoreactivity. *Nat. Chem.* **2021**, *13*, 956–962.
- (62) Lowry, M. S.; Bernhard, S. Synthetically tailored excited states: phosphorescent, cyclometalated iridium(III) complexes and their applications. *Chem.—Eur. J.* **2006**, *12* (31), 7970–7977.
- (63) Lowry, M. S.; Hudson, W. R.; Pascal, R. A.; Bernhard, S. Accelerated Luminophore Discovery through Combinatorial Synthesis. *J. Am. Chem. Soc.* **2004**, *126*, 14129–14135.
- (64) Wu, S.; Ling, J.; Lai, S.; Huang, M.; Cheng, C. H.; Chen, I. Dynamics of the Excited States of [Ir(ppy)₂bpy]⁺ with Triple Phosphorescence. *J. Phys. Chem. A* **2010**, *114* (38), 10339–10344.
- (65) Deaton, J. C.; Castellano, F. N. Archetypal Iridium(III) Compounds for Optoelectronic Applications Photophysical Properties and Synthetic Methods, 1st ed.; John Wiley & Sons Ltd: Hoboken, NJ, 2017.
- (66) Monti, F.; Baschieri, A.; Sambri, L.; Armaroli, N. Excited-State Engineering in Heteroleptic Ionic Iridium(III) Complexes. *Acc. Chem. Res.* **2021**, 54 (6), 1492–1505.
- (67) Sajoto, T.; Djurovich, P.; Tamayo, A.; Oxgaard, J.; Goddard, W.; Thompson, M. Temperature Dependence of Blue Phosphorescent Cyclometalated Ir(III) Complexes. *J. Am. Chem. Soc.* **2009**, *131*, 9813–9822.
- (68) Scattergood, P. A.; Ranieri, A. M.; Charalambou, L.; Comia, A.; Ross, D. A. W.; Rice, C. R.; Hardman, S. J. O.; Heully, J. L.; Dixon, I. M.; Massi, M.; Alary, F.; Elliott, P. I. P. Unravelling the Mechanism of

- Excited-State Interligand Energy Transfer and the Engineering of Dual Emission in $[Ir(C-N)_2(N-N)]^+$ Complexes. *Inorg. Chem.* **2020**, *59* (3), 1785–1803.
- (69) Brooks, A. C.; Basore, K.; Bernhard, S. Photon-Driven Reduction of Zn²⁺ to Zn Metal. *Inorg. Chem.* **2013**, *52* (10), *5794*–*5800*.
- (70) DiLuzio, S.; Mdluli, V.; Connell, T. U.; Lewis, J.; VanBenschoten, V.; Bernhard, S. High-Throughput Screening and Automated Data-Driven Analysis of the Triplet Photophysical Properties of Structurally Diverse, Heteroleptic Ir(III) Complexes. *J. Am. Chem. Soc.* **2021**, *143* (2), 1179–1194.
- (71) Mdluli, M.; DiLuzio, S.; Lewis, J.; Kowalewski, J.; Connell, T.; Yaron, D.; Kowalewski, T.; Bernhard, S. High-throughput Synthesis and Screening of Iridium(III) Photocatalysts for the Fast and Chemoselective Dehalogenation of Aryl Bromides. *ACS Catal.* **2020**, *10* (13), 6977–6987.
- (72) Lopato, E. M.; Eikey, E. A.; Simon, Z. C.; Back, S.; Tran, K.; Lewis, J.; Kowalewski, J. F.; Yazdi, S.; Kitchin, J. R.; Ulissi, Z. W.; Millstone, J. E.; Bernhard, S. Parallelized Screening of Characterized and DFT-Modeled Bimetallic Colloidal Cocatalysts for Photocatalytic Hydrogen Evolution. ACS Catal. 2020, 10 (7), 4244–4252.
- (73) Masood, H.; Toe, C. Y.; Teoh, W. Y.; Sethu, V.; Amal, R. Machine Learning for Accelerated Discovery of Solar Photocatalysts. *ACS Catal.* **2019**, 9 (12), 11774–11787.
- (74) Westermayr, J.; Marquetand, P. Machine Learning for Electronically Excited States of Molecules. *Chem. Rev.* **2021**, *121* (16), 9873–9926.
- (75) Buglioni, L.; Raymenants, F.; Slattery, A.; Zondag, S. D. A.; Noel, T. Technological Innovations in Photochemistry for Organic Synthesis: Flow Chemistry, High-Throughput Experimentation, Scale-up, and Photoelectrochemistry. *Chem. Rev.* **2021**, DOI: 10.1021/acs.chemrev.1c00332.
- (76) Bai, Y.; Wilbraham, L.; Slater, B. J.; Zwijnenburg, M. A.; Sprick, R. S.; Cooper, A. I. Accelerated Discovery of Organic Polymer Photocatalysts for Hydrogen Evolution from Water through the Integration of Experiment and Theory. J. Am. Chem. Soc. 2019, 141 (22), 9063–9071.
- (77) Turro, N. Photochemical Reactivity. J. Chem. Educ. 1967, 44 (9), 536–537.
- (78) Tinker, L. L.; McDaniel, N. D.; Curtin, P. N.; Smith, C. K.; Ireland, M. J.; Bernhard, S. Visible light induced catalytic water reduction without an electron relay. *Chem.—Eur. J.* **2007**, *13* (31), 8726–8732.
- (79) DiSalle, B. F.; Bernhard, S. Orchestrated photocatalytic water reduction using surface-adsorbing iridium photosensitizers. *J. Am. Chem. Soc.* **2011**, *133* (31), 11819–11821.
- (80) Mishra, A.; DiLuzio, S.; Alahbakhshi, M.; Adams, A.; Bowler, M.; Moon, J.; Gu, Q.; Zakhidov, A.; Bernhard, S.; Slinker, J. *Chem. Mater.* **2021**, 33 (4), 1201–1212.
- (81) Bevernaegie, R.; Wehlin, S. A. M.; Piechota, E. J.; Abraham, M.; Philouze, C.; Meyer, G. J.; Elias, B.; Troian-Gautier, L. Improved Visible Light Absorption of Potent Iridium(III) Photo-oxidants for Excited-State Electron Transfer Chemistry. *J. Am. Chem. Soc.* **2020**, 142 (6), 2732–2737.
- (82) Neumann, S.; Wenger, O.; Kerzig, C. Controlling Spin-Correlated Radical Pairs with Donor-Acceptor Dyads: A New Concept to Generate Reduced Metal Complexes for More Efficient Photocatalysis. *Chem.—Eur. J.* **2021**, 27, 4115–4123.
- (83) Sayre, H.; Ripberger, H. H.; Odella, E.; Zieleniewska, A.; Heredia, D. A.; Rumbles, G.; Scholes, G. D.; Moore, T. A.; Moore, A. L.; Knowles, R. R. PCET-Based Ligand Limits Charge Recombination with an Ir(III) Photoredox Catalyst. *J. Am. Chem. Soc.* **2021**, *143* (33), 13034–13043.
- (84) Yang, M.; Yarnell, J. E.; El Roz, K.; Castellano, F. N. A Robust Visible-Light-Harvesting Cyclometalated Ir(III) Diimine Sensitizer for Homogeneous Photocatalytic Hydrogen Production. *ACS Appl. Energy Mater.* **2020**, 3 (2), 1842–1853.
- (85) Ruccolo, S.; Qin, Y.; Schnedermann, C.; Nocera, D. General Strategy for Improving the Quantum Efficiency of Photoredox Hydroamidation Catalysis. *J. Am. Chem. Soc.* **2018**, *140*, 14926–14937.

- (86) Aydogan, A.; Bangle, R.; Cadranel, A.; Turlington, M.; Conroy, D.; Cauët, E.; Singleton, M.; Meyer, G.; Sampaio, R.; Elias, B.; Troian-Gautier, L. Accessing Photoredox Transformations with an Iron(III) Photosensitizer and Green Light. *J. Am. Chem. Soc.* **2021**, *143* (38), 15661–15673.
- (87) Jayanthi, S.; Ramamurthy, P. Photoinduced electron transfer reactions of 2,4,6-triphenylpyrylium: solvent effect and charge-shift type of systems. *Phys. Chem. Chem. Phys.* **1999**, *1*, 4751–4757.
- (88) Olmsted, J.; Meyer, T. Factors Affecting Cage Escape Following Electron-Transfer Quenching. *J. Phys. Chem.* **1987**, *91*, 1649–1655.
- (89) Georgopoulos, M.; Hoffman, M. Cage Escape Yields in the Queching of *Ru(bpy)₃²⁺ by Methylviologen. Presence of Triethanolamine as a Sacrificial Electron Donor. *J. Phys. Chem.* **1991**, 95, 7717–7721.
- (90) Arias-Rotondo, D. M.; McCusker, J. K. The photophysics of photoredox catalysis: a roadmap for catalyst design. *Chem. Soc. Rev.* **2016**, 45 (21), 5803–5820.
- (91) Sun, H.; Neshvad, G.; Hoffman, M. Z. Energy Gap Dependence of the Efficiency of Charge Separation upon the Sacrificial Reductive Quenching of the Excited States of Ru(II)-Diimine Photosensitizers in Aqueous Solution. *Mol. Cryst. Liq.* **1991**, *194* (1), 141–150.
- (92) Zhao, H.; Leonori, D. Minimization of Back-Electron Transfer Enables the Elusive sp³ C-H Functionalization of Secondary Anilines. *Angew. Chem., Int. Ed.* **2021**, *60* (14), 7669–7674.
- (93) Oppelt, K.; Fernández-Terán, R.; Pfister, R.; Hamm, P. Geminate Recombination versus Cage Escape in the Reductive Quenching of a Re(I) Carbonyl Complex on Mesoporous ZrO₂. *J. Phys. Chem. C* **2019**, 123 (32), 19952–19961.
- (94) Barry, J. T.; Tyler, D. R. Solvent Cage Effects: A Comparison of Geminate and Nongeminate Radical Cage Pair Combination Efficiencies. *Inorg. Chem.* **2020**, *59* (19), 13875–13879.
- (95) Gould, I.; Ege, D.; Moser, J.; Farid, S. Efficiency of Photoinduced Electron-Transfer Reactions: Role of the Marcus Inverted Region in Return Electron Transfer with Geminate Radical-Ion Pairs. *J. Am. Chem. Soc.* **1990**, *112*, 4290–4301.
- (96) Brunschwig, B. S.; Ehrenson, S.; Sutin, N. The distance dependence of electron transfer reactions: rate maxima and rapid rates at large reactant separations. *J. Am. Chem. Soc.* **1984**, *106* (22), 6858–6859.
- (97) Sutin, N.; Creutz, C. Electron-transfer reactions of excited state. *J. Chem. Educ.* **1983**, *60* (10), 809–814.
- (98) Pellegrin, Y.; Odobel, F. Sacrificial electron donor reagents for solar fuel production. C. R. Chim. 2017, 20, 283–295.